Published in final edited form as:
J Adhes Sci Technol. 2013 February 1; 27(3): 227–243. doi:10.1080/01694243.2012.705101.

The Effects of Geometry on Skin Penetration and Failure of Polymer Microneedles

Shaun D Gittard[1,2,*], **Bo Chen**[1], **Huadong Xu**[1], **Aleksandr Ovsianikov**[2], **Boris N Chichkov**[2], **Nancy A Monteiro-Riviere**[1,3], and **Roger J Narayan**[1,**]

[1]Joint Department of Biomedical Engineering, North Carolina State University, Raleigh, NC 27695, USA

[2]Laser Zentrum Hannover, Hollerithalle 8, 30419 Hannover, Germany

[3]Center for Chemical Toxicology Research and Pharmacokinetics, North Carolina State University, Raleigh, NC 27607, USA

Abstract

Microneedles are small-scale devices that may be used for drug delivery and biosensing. In this study, the forces required for mechanical failure, the modes of mechanical failure, as well as the mechanisms for microneedle penetration into porcine skin were examined. Microneedles produced from the acrylate-based polymer e-Shell 200 using an indirect rapid prototyping approach involving two-photon polymerization and poly(dimethylsiloxane) micromolding were found to possess sufficient strength for penetration of porcine skin. The failure forces were an order of magnitude greater than the forces necessary for full insertion into the skin. Bending was the most common form of failure; an increasing aspect ratio and a decreasing tip diameter were associated with lower failure forces. Video captured during skin penetration revealed that microneedle penetration into the skin occurred by means of a series of insertions and not by means of a single insertion event. Images obtained during and after skin penetration confirmed microneedle penetration of skin as well as transdermal delivery of lucifer yellow dye. These findings shed insight into the mechanisms of microneedle penetration and failure, facilitating design improvements for polymer microneedles.

Keywords

microneedle; micromolding; acrylate-based polymer; porcine skin

1. Introduction

Over time, nature has developed numerous forms of attachment structures [1]. For example, Stork evaluated the ability of insects, lizards, and spiders to attach and subsequently detach from a given surface in a reversible manner [2–3]. Many insects, lizards, and spiders possess adhesive pads; these structures contain flexible micrometer- or nanometer-sized hairy structures that are known as setae [1–11]. These structures have independently evolved in insects, lizards, and spiders [7, 10, 11]. Lizard, spider, and fly setae exhibit surprisingly similar features, including brushlike morphologies, contact elements, terminal elements (e.g., spatulae), and other ultrastructural features. Natural selection has also led to the development of structures for penetration of dense structures. For example, the woodpecker beak exhibits a unique geometry for penetrating wood that facilitates acquisition of insects

---

*Corresponding authors shaun.gittard@gmail.com. **roger_narayan@unc.edu.

under tree bark [12]. Free body analysis studies have indicated that beak geometry correlates with forces on the structure during drilling. The fascicle of a mosquito is a structure developed by natural selection for penetration of animal skin or human skin. Fascicles are 30 μm wide and 2 mm long needle-like structures, which are used by female mosquitoes to penetrate the skin and obtain blood [13, 14].

The spines and thorns on the surfaces of plants as well as the fascicles of mosquitoes have been imitated in microneedle devices for transdermal sensing and drug delivery [15–31]. For example, an indirect rapid prototyping approach involving two-photon polymerization and micromolding may be used to create microneedles [32]. This approach enables facile and rapid fabrication of multiple microneedles or other three-dimensional structures of a given geometry for mechanical testing. LaFratta et al. created microscale interlocking rings, arches, bridges, cantilevers, and coils by means of multiphoton absorption polymerization and microtransfer molding [33]. Lim et al. created replicas of three-dimensional hemisphere and pyramid structures by means of two-photon polymerization and microtransfer molding [34]. Mukai et al. utilized a combination of photopolymerization and molding to create three-dimensional rice grain-shaped structures [35]. Sun et al. used two-photon polymerization/micromolding to fabricate micro gears out of polycarbonate and poly (methyl methacrylate) [36]. More recently, Koroleva et al. used microreplication molding in order to replicate two-photon polymerization-fabricated tissue engineering scaffolds with thin walls and overhanging features [37]. Gittard et al. prepared solid microneedle arrays from a photosensitive acrylate-based polymer using two-photon polymerization microfabrication in combination with poly(dimethylsiloxane) micromolding [38]. They created microneedles from e-Shell 200 (EnvisionTEC, Gladbeck, Germany), a photosensitive acrylate-based polymer containing 78% carbon, 20% oxygen, and 2% titanium [38]. This material is described as a Class-IIa biocompatible material as per the ISO 10993 regulation [38]. The e-Shell 200 material exhibited resistance to perspiration as well as water; it is utilized in hearing aid shells and other medical devices. As per the manufacturer-supplied technical data, e-Shell 200 exhibits a hardness of 83 Shore, a flexural modulus of 2,300 MPa, a flexural strength of 103 MPa, a modulus of elasticity of 2,400 MPa, and a tensile strength of 57.8 MPa [39]. In their work, Gittard et al. performed limited mechanical testing; examination on only one microneedle geometry was carried out.[38] A five-by-five e-Shell 200 microneedle withstood a 10 N axial load, corresponding to 0.4 N/microneedle. In addition, linearity of the force- displacement curve was noted for 4–10 N axial loads, suggesting elastic deformation over these values. In another study, the Young's modulus and hardness values of polymerized e-Shell 200 material were determined by nanoindentation to be 3050 +/− 90 MPa and 93.8 +/− 7.25 MPa, respectively [40]. Two-photon polymerization/micromolding was also used to create microneedles containing gentamicin or silver, which exhibited antimicrobial properties against *Staphyloccous aureus* [41, 42].

Several investigators have examined the mechanical properties of microneedles. For example, Davis et al. investigated the relationship between the fracture force of nickel microneedles and several parameters, including wall thickness, wall angle, and tip radius [43]. In this study, the relationships between these geometric factors and penetration force were evaluated. Aoyagi et al. measured the effects of tip angle and width on insertion force using poly(lactic acid) microneedles [26]. Park et al. examined the effect of microneedle tip area on the ability to penetrate the stratum corneum; they noted that microneedles with smaller tip areas required lower penetration forces [44]. This study also examined the relationships between several geometric factors and the mechanical properties of microneedles; failure forces were examined in both axial and transverse directions. Kim et al. examined penetration of skin by arrays of out-of -plane hollow silicon dioxide microneedles with several cross-sections and widths [45]. Khanna et al. showed that sharpening hollow silicon microneedles only at the tip resulted in lower human cadaver skin insertion forces. Since the sharpened microneedle shaft exhibited the same diameter as the unsharpened microneedle shaft, the mechanical strength of the microneedle was retained [46]. Their work indicated that human skin exhibited a toughness of 24.28 kJ m^{-2}. In another study, Khanna et al. prepared hollow microneedles with 35 gauge and 36 gauge features [47]. In this study, microneedles with two lumen geometries were created; microneedles with an enhanced 'letter I' shaped lumen geometry were shown to possess higher strength than those with a conventional circular lumen geometry. The I-shaped microneedles were shown to possess higher shear fracture limits than the conventional microneedles in the lateral direction and lower shear fracture limits than the conventional microneedles in the transverse direction. They also noted that the geometrical contribution to shear strength was greater for microneedles with smaller dimensions.

Although numerous studies have examined the mechanical properties of microneedles, several factors have yet to be examined. Since skin exhibits viscoelastic behavior, bending of the skin occurs during microneedle insertion [43, 48]. In addition, the surface of skin has a nonuniform topology, which can affect penetration depth measurements. Examining the depth of penetration for microneedles and the mechanism by which microneedles enter the skin beyond the stratum corneum are necessary steps for enabling researchers to better understand how pharmacological agents and vaccines are delivered using microneedles.

The most common techniques for determining skin penetration are transepidermal water loss (TEWL) [49–51], electrical resistance [43, 44, 52], and post-penetration staining [49]. In TEWL measurements, the rate of total amount of water vapor loss through the skin is determined; the TEWL increases when the stratum corneum barrier, which prevents diffusion and evaporation of water, is compromised. The stratum corneum is non-conducting since it contains keratinized cells and does not contain water. The electrical resistance is significantly lower in lower layers of skin, which contain living cells. In order to determine stratum corneum penetration, dyes that stain cells in the epidermis but not in the stratum corneum can be topically applied after microneedle application. If the stratum corneum has been compromised, the dyes will be able to stain the epidermis in the region surrounding the microneedle-generated pores. Numerous dyes have been used to examine microneedle delivery properties, including trypan blue, methylene blue, and gentian violet [49, 53–55]. These techniques have several shortcomings when used for evaluating microneedle penetration. Most importantly, these techniques verify that the stratum corneum has been breached but do not indicate the depth of microneedle penetration. In many applications (e.g., delivery of pharmacological agents that require rapid biodistribution), the depth of microneedle penetration is an important parameter. Al-Qallaf and Das developed a detailed model to determine the relationships between microneedle array design and drug delivery properties [56]. In their model, the microneedles were shown to completely penetrate into the skin; calculations of drug permeation were based on factors such as microneedle base radius and microneedle length. If the microneedles are not fully penetrated into the skin, then these values will need to be adjusted to reflect the apparent radius and the apparent length of the microneedle that is actually located in the epidermis. In this study, we examined the mechanical properties of e-Shell 200 acrylate-based polymer solid microneedles with a variety of geometries. The purpose of this study was two-fold: to better understand the mechanical properties of e-Shell 200 microneedles and to better understand the mechanisms of skin penetration by microneedles. Compression of microneedles was performed while recording force, displacement, and video data. Delivery of lucifer yellow dye from the microneedles into the surrounding region of the skin was also demonstrated using fluorescence microscopy techniques.

2. Materials and Methods

Master structures of the needles were made using two-photon polymerization. A Ti:sapphire femtosecond laser (Chameleon, Coherent, Santa Clara, CA), which was operated with λ=780 nm and 60 fs pulses, was used to selectively polymerize a photosensitive resin. Poly(ethylene glycol diacrylate) (molecular weight 302) (SR259, Sartomer, Paris, France) with 2% wt of the photoinitiator Irgacure 369 (Ciba Specialty Chemicals, Basel, Switzerland) was the photosensitive resin that was used in this study. Structuring of the photosensitive resin was performed by focusing the laser with a 5× objective and a numerical aperture of 0.13 (Zeiss, Jena, Germany). A hurrySCAN® scan head (Scanlabs, Puchheim, Germany) was used to control the lateral dimensions of the laser; a translational stage (C-843, Physik Instrumente, Karlsruhe, Germany) was used to control the height of the focal plane of the laser within the resin. The laser was guided using .STL files; custom-written software sliced the file into layers and rastered the laser across the contour of each layer. After structuring of the photosensitive resin, the unpolymerized resin was removed by washing in ethanol. Exposure to an ultraviolet lamp after washing ensured that the structures were completely polymerized. Input .STL files for the needles were produced using Solidworks Education Edition 2009 (Dassault Systemes SA, Velizy, France). Microneedles were prepared in three different geometries; information on microneedle geometries is provided in Table 1.

Mass replication of the master structures was achieved by poly(dimethylsiloxane) micromolding; this process has been previously described [38]. The master structures were coated with gold by sputter coating and were then molded with a thick layer of poly(dimethylsiloxane) (PDMS) (Sylgard® 184, Dow Corning, Midland, MI). The molds and master structures were separated using a linear translational stage. Replicas were created by filling the mold with e-Shell 200 liquid resin (EnvisionTEC GmbH, Gladbeck, Germany) using greater than 1 mbar vacuum. Polymerization of the microneedles was achieved using a UV flash oven (Otoflash, EnvisionTEC GmbH, Gladbeck, Germany). The replicas were then manually separated from the molds.

Scanning electron microscopy imaging of the poly(dimethylsiloxane) micromolding-produced microneedles was obtained using a variable pressure S3200 instrument (Hitachi, Tokyo, Japan). Images of the microneedles after compression and skin penetration were acquired using an EZ 4 dissection microscope (Leica, Wetzler, Germany). Videos during compression and skin penetration testing were captured with a commercially-available CCD camera, which was focused using a 10× objective.

Compression of the microneedles was performed using an Electroforce 3100 instrument with a 20 N load cell and WinTest® software (Bose, Eden Prairie, MN); this instrument provides 1 mN force resolution and 0.001 mm displacement resolution. Microneedles of all three geometries were compressed to loads of 0.1 N, 0.25 N, 0.5 N, 0.75 N, and 1 N in a load controlled mode at a rate of 0.001 N/s. Load and displacement were recorded during compression testing. Full-thickness porcine skin was used for examining skin penetration of the microneedles. Microneedles with all three geometries were pressed into full-thickness skin using the load cell. Penetration was performed using a displacement controlled mode; a rate of 0.01 mm/s and a total displacement of at least 1.3 mm were utilized in this study.

Drug delivery studies were performed using microneedles with geometry A that were coated with lucifer yellow dye (Thermo Fisher Scientific, Waltham, MA). Lucifer yellow was chosen due to the fact that it exhibits minimal diffusion in tissue; it is a hydrazine-derivative dye that covalently interacts with proteins. Coating was performed by placing a 0.1 mL droplet of a 5% lucifer yellow solution in water onto the microneedle structure; the solvent was evaporated by heating at 60° C for 15 minutes. The microneedles were pressed into porcine skin by hand for fifteen minutes and subsequently imaged. Images of the microneedle-produced pores at the surface of the skin were obtained by removing the microneedle array; widefield fluorescence imaging by means of a TC-5500 epi-fluorescent microscope (Meiji Techno America, Santa Clara, CA) was performed.

Confocal microscopy was used to confirm that the lucifer yellow dye was delivered below the surface of the skin. Prior to imaging, needles were pressed into the skin for fifteen minutes and subsequently removed. An LSM 710 microscope (Carl Zeiss, Oberkochen, Germany) was used to obtain differential interference contrast (DIC) and fluorescence images of the microneedle-produced pores at a location 100 μm below the surface of the skin. In this study, excitation was obtained with a 458 nm laser and emission was collected between 494 and 600 nm. Microneedles in the skin were imaged with multiphoton microscopy via an LSM 710 NLO microscope (Carl Zeiss, Oberkochen, Germany); excitation at 740 nm was provided by a Chameleon femtosecond laser (Coherent, Santa Clara, CA). A beam splitter was used to collect emission below 690 nm. For multiphoton microscopy imaging, the microneedles were left in the skin while the images were obtained. Fluorescence from the dye was imaged from the surface of the skin to 100 μm below the surface of the skin in order to determine how much of the microneedle was located in the skin.

3. Results

Scanning electron microscopy confirmed that poly(dimethylsiloxane) micromolding produced accurate replicas of the microneedle structures. A characteristic scanning electron microscopy image of a replicated microneedle (geometry B) is provided in Figure 1. The bodies of all of the microneedles exhibited surfaces with smooth features; radii of tip curvature values for the microneedles are shown in Table 1. In addition to microneedle dimensions, mechanical properties of the microneedles are summarized in Table 1. The linear regions of the force versus displacement data were used to calculate the average stiffness values; data from four compression studies for each of the microneedle geometries were used. The average stiffness values were 1620 N/m, 2222 N/m, and 7580 N/m for microneedle geometries A, B, and C, respectively. The average displacement values for the microneedles after 0.1 N and 0.2 N of compression are also provided in Table 1.

The microneedle geometries underwent compression with forces ranging from 0.1 N to 1.0 N. Optical microscopy images of the microneedles after compression to this range of forces are provided in Figure 2. All three geometries were able to sustain forces up to 0.1 N without any visual signs of damage. At 0.25 N force, slight deformation of the tip of the microneedle with geometry A (3:1 aspect ratio) was observed; on the other hand, microneedles with geometries B and C showed no signs of damage. At forces of 0.5 N and higher, permanent tip deformation of microneedles with geometries B and C was observed. During 10% of compressions above 0.1 N, the microneedle with geometry A exhibited fracture near the tip; the other 90% of the compressions resulted in bending or compressing followed by bending. Microneedles with geometry B exhibited bending of the tip. Microneedles with geometry C underwent compression of the tip; bending was observed at forces greater than 0.75 N.

Characteristic force versus displacement plots for the three microneedles are provided in Figure 3a. The mechanical strength values for the microneedles were noted to be inversely related to aspect ratio. The microneedles with geometry C (2:1 aspect ratio) underwent less than 0.1 mm of deformation with 0.75 N of force; on the other hand, the microneedles with geometry B (2.5:1 aspect ratio) and geometry C (3:1 aspect ratio) underwent approximately

0.25 mm and 0.33 mm of deformation at 0.75 N, respectively. Figure 3b contains characteristic plots of the three failure mechanisms occurring in the microneedles; all of these curves were obtained from compression testing of microneedles with geometry A. Fracture of the microneedle tip was associated with a sharp spike in the force versus displacement curve. Compression of the microneedle tip resulted in an approximately linear relationship; on the other hand, bending produced a shoulder in the force versus displacement plot. Characteristic plots of force and displacement versus time in load controlled mode are provided in Figure 4. A microneedle with geometry B undergoing bending is represented in Figure 4a. The load curve is linear; a shoulder in the displacement curve was noted when bending of the microneedle took place. Eventually, displacement resumed linear behavior as the compression platen reached a portion of the microneedle with a sufficiently larger diameter; at this point, bending no longer occurred. Fracture of a microneedle is presented in Figure 4b; fracture was associated with a sharp spike in the load curve and a simultaneous rise in displacement.

Penetration of microneedles into full-thickness porcine skin was achieved without damage for microneedles with all three geometries. Images of the three needle geometries after insertion into skin with 1.0 N of force are presented in Figure 5. Figure 6 contains force versus displacement curves for microneedles with the three geometries penetrating into skin in displacement control mode. No significant differences between the penetration forces for microneedles with the three geometries were observed. Figure 7 provides a characteristic comparison (geometry B) of microneedle penetration into skin versus compression. Microneedle penetration into the skin takes place with significantly less force than what is associated with microneedle damage.

Video footage showing microneedle compression and penetration into skin was collected simultaneously with force and displacement measurements. Screenshots of microneedle compression and penetration, both obtained using microneedles with geometry B, were produced from these videos to facilitate visualization. Figure 8 contains screenshots of a characteristic microneedle compression (geometry B) in load controlled mode; the corresponding displacement and load versus time plots are shown underneath. The microneedle can be seen to bend at the tip and along the base; partial recovery was noted after the force had been released. Video data and the corresponding mechanical data for a characteristic microneedle penetration into skin in displacement controlled mode are provided in Figure 9; data for a microneedle with geometry B are shown. The mechanical data and video data both indicate that penetration of the microneedle into the skin consists of an incremental series of skin bending events; partial rebounding was noted upon deeper piercing of the microneedle. The skin was noted to rebound upward from the 24 second frame to the 25 second frame.

Fluorescence microscopy confirmed that the coated microneedles created pores in the skin and delivered lucifer yellow dye. After microneedle removal, brightfield fluorescence microscopy and confocal microscopy confirmed the presence of pores 120 μm below the skin surface and at the skin surface (Figure 10). The microneedle-produced pores were significantly smaller than the microneedle dimensions; in addition, the microneedle-produced pores were noted to possess irregular shapes. Confocal microscopy also confirmed delivery of the lucifer yellow dye into the surrounding region of the skin.

Multiphoton microscopy data were collected from the surface of the skin to a 100 μm depth in the skin in order to determine the degree of tenting of the skin (Figure 11). The microneedle-produced pores were noted to possess a regular circular shape from 96 μm deep to 36 μm deep. From 36 μm to the surface of the skin, the microneedle-produced pores were noted to possess an irregular shape. The diameter of the microneedle-produced pore at a depth of 36 μm from the surface of the skin was 221 μm; the base diameter of the microneedle was 250 μm. The microneedle with geometry A exhibited a diameter of 221 μm at a depth of 86 μm from the base; 664 μm or 88.5% of the length of the microneedle resided in the skin.

4. Discussion

Scanning electron microscopy confirmed that poly(dimethylsiloxane) micromolding is an appropriate technique for mass producing replicas of small-scale structures, such as those produced by two-photon polymerization. This technique has previously been used to mass produce replicas of microscale structures that were generated using a variety of techniques, including two-photon polymerization [38, 41, 42], laser ablation [37], and reactive ion etching[53]. The microneedles produced from the polymer e-Shell 200 were found to be remarkably strong. The stiffness values of all three microneedle geometries were greater than 1600 N/m; stiffness was noted to increase with decreasing aspect ratio. Microneedles with all three geometries were able to undergo 0.1 N of compressive force without permanent tip deformation for an individual microneedle. The weakest microneedle, the microneedle with geometry A, only displaced 0.127 mm with 0.1 N of compression and displaced 0.182 mm with 0.2 N of compression. Lee et al. reported failure of poly(lactic-co-glycolic acid) microneedles with similar geometries; failure forces from 0.06 N to 0.25 N were noted [57].

Mechanical strength of the microneedles was found to be significantly affected by geometry. Stiffness increased from 1620 N/m for microneedles with geometry A (3:1 aspect ratio) to more than 7500 N/m for microneedles with geometry C (2:1 aspect ratio), a more than four-fold increase. Likewise, displacement under 0.2 N of compression decreased from 0.182 mm for microneedles with geometry A to only 0.042 mm for microneedles with geometry C, a more than four-fold difference. The tip diameters were noted to be higher in microneedles that exhibited smaller aspect ratio values. Therefore, it is not possible to differentiate between the effects of these two geometric factors. Davis et al. reported that increasing tip diameter and decreasing aspect ratio in microneedles both resulted in increased mechanical strength; their result is in agreement with our data [43].

The primary mechanism of failure for the microneedles was compression followed by bending. Elastic bending of the microneedle initially occurred; this phenomenon was followed by plastic bending of the microneedle. As the aspect ratio was increased, the force required for elastic and plastic bending decreased. The microneedle with geometry A (3:1 aspect ratio) began plastic bending beyond 0.1 N, the microneedle with geometry B (2.5:1 aspect ratio) exhibited plastic bending beyond 0.25 N, and the microneedle with geometry C (2:1 aspect ratio) exhibited plastic bending beyond 0.75 N. Fracture of the highest aspect ratio microneedles, those with geometry A (3:1), occurred 10% of the time; fracture always occurred after plastic bending had begun. Fracture always occurred near the tip of the microneedles at the point where the most bending had already taken place. The failure mechanism of polymer microneedles is favorable in comparison to that of ceramic microneedles or silicon microneedles.

All of the microneedle geometries were able to penetrate the skin with exceptionally low forces; all three of the microneedle geometries had displaced more than 0.5 mm into the skin before forces greater than 5 mN were achieved. Beyond a displacement of 0.75 mm, the forces for microneedles with geometry C were noted to significantly increase; this increase was attributed to compression of the skin resulting from substrate-skin contact. In comparison, blunt-tipped microneedles investigated by Davis et al. demonstrated piercing of the stratum corneum by means of electrical conduction at approximately 0.5 N [43]. These blunt-tipped microneedles also displaced the skin approximately 500 μm before stratum corneum piercing was achieved. In their work, the microneedles were produced from metal; the failure mechanism of the microneedles was by fracturing and buckling. Another important factor to note about skin penetration is that the forces applied to the microneedle during compression and during penetration do not exactly correspond. During compression into a hard surface, the entire applied force is on the surface of the microneedle. In contrast, forces during skin penetration are distributed over a larger area of the microneedle, particularly after initial penetration.

No significant differences in the penetration properties of the microneedles with the three geometries were observed. In comparison, differences in geometry were found to have a significant effect on the mechanical strength of the microneedles. The 2:1 aspect ratio would be the best geometry for clinical use; it exhibits higher strength without a significantly different penetration force. The 2:1 aspect ratio needle has the highest margin of safety. Based on the data obtained, all three geometries would be considered to be safe for use in drug delivery. It should be noted that the force required for compressing 1 mm into the skin (~0.015 N) is an order of magnitude less than the force at which plastic deformation occurs (~0.2 N) for the microneedle with the 3:1 aspect ratio geometry.

Information about microneedle penetration into skin was obtained from video footage and mechanical measurements that were acquired during microneedle penetration. Both the recorded mechanical data and the video indicated that there was not a singular force at which microneedles penetrated the skin; instead, a series of increasing forces was required for the microneedles to penetrate more deeply into the skin. Upon application of the microneedles to the skin, the skin became compressed until a threshold was reached; above this threshold, the microneedle began piercing through the tissue. In the video data, piercing can be observed when the skin rebounds towards the needles. Piercing was associated with a sharp drop in force. In the video of skin penetration, the skin was noted to rebound frequently at the beginning of skin penetration. The entire skin was shown to rebound, with hairs aiding in visualization of skin motion. These findings indicate that there is not a singular force required for a microneedle to penetrate the skin; instead, a threshold force is required for a microneedle to pierce the skin to a certain depth. Numerous studies have reported a singular force at which the needle is inserted into the skin. Davis et al. [43] and Choi et al. [52] reported singular forces of insertion, which they determined via the decrease in resistance when the stratum corneum was compromised. Techniques that indicate if the stratum corneum has been compromised (e.g., TEWL measurements and staining) provide only partial information about microneedle penetration. In order to form accurate pharmacological models of drug delivery via microneedles, the depth of release for the pharmacological agent or vaccine must be known. Consequently, TEWL and staining do not provide complete information for assessing microneedle-based drug delivery into the skin. Imaging techniques are better suited for determining the depth of penetration into the skin; however, development of additional methods for imaging microneedle-based drug delivery into skin are necessary [42, 58–62].

Microneedle penetration of the skin was further confirmed by examining microneedles in porcine skin and after removal of microneedles from porcine skin. Fluorescence microscopy also confirmed that a model drug, lucifer yellow, had been delivered into the skin. The microneedle-produced pores were found to remain in the skin after microneedle removal. The irregular dimensions of the microneedle-produced pores were associated with anisotropic tensile forces, which were associated with elastic and collagen fibers within the skin. These pores may be used for delivery of pharmacological agents or vaccines after removal of the microneedle device from the skin. Previous work by Gittard et al. noted similar pore shapes in microneedle-treated human stratum corneum and epidermis after microneedle removal [38]. Comparable results were noted by Park et al. for penetration of human cadaver skin by poly(L-glycolic acid) microneedles [63].

Multiphoton microscopy indicated slight tenting of the skin in the region surrounding the microneedle base. Tenting was present in the upper 36 μm; in this region, the pore was noted to be irregular in shape. At lower depths, the pore was noted to be isotropic, indicating that no tenting had occurred at these depths. By measuring the diameter of the pore at the location at which tenting no longer occurred, the length of the microneedle residing in the skin was determined. 88.5% of the length of the microneedle with geometry A (86 μm) was found to penetrate the skin. In contrast, blunt-tipped needles have been associated with tenting on the order of hundreds of micrometers [43].

5. Conclusions

Microneedles produced from the acrylate-based polymer e-Shell 200 were shown to possess appropriate material properties for use in transdermal drug delivery. All three of the investigated microneedle geometries were able to penetrate skin; the forces for skin penetration were at least an order of magnitude less than the forces at which damage to the microneedles took place. Geometry was shown to have a significant effect on the mechanical strength of the microneedles; a decrease in aspect ratio corresponded to an increase in microneedle mechanical strength. Observation of skin penetration revealed that microneedle piercing of the skin was not a single event; instead, a series of penetrations occurred in which the microneedles progressively pierced more deeply into the skin. Various microscopic methods confirmed that the microneedles were able to deliver a model drug, lucifer yellow, into the skin. These findings show that an indirect rapid prototyping involving two-photon polymerization and poly(dimethylsiloxane) micromolding is an effective means of mass producing acrylate-based polymer microneedles for transdermal drug delivery. Furthermore, we have shown that an effective means of determining the location of the microneedle within the skin is necessary since the depth of microneedle penetration into the skin is dependent on the applied force.

6. References

1. Haas F, Gorb S. Arthropod Structure Development. 2004; 33:45. [PubMed: 18089022]
2. Stork NE. J. Natural History. 1983; 17:583.
3. Stork NE. J. Natural History. 1983; 17:829.
4. Langer MG, Ruppersberg JP, Gorb S. Proc. Royal Soc. 2004; 271:2209.London Series B
5. Arzt E, Gorb S, Spolenak R. Proc. Natl. Acad. Sci. USA. 2003; 100:10603. [PubMed: 12960386]
6. Persson BNJ, Gorb S. J. Chem. Phys. 2003; 119:11437.
7. Williams EE, Peterson JA. Science. 1982; 215:1509. [PubMed: 17788677]
8. Betz O. J. Morphology. 2003; 255:24.
9. Gorb SN. Proc. Royal Soc. 1998; 265:747.London Series B
10. Coddington JA, Levi HW. Annual Review Ecology Systematics. 1991; 22:565.
11. Irschick DJ, Austin CC, Petren K, Fisher RN, Losos JB, Ellers O. J. Linnean Society. 1996; 59:21.
12. Bock WJ. Ostrich. 1999; 70:23.
13. Mellink JJ, van den Bovenkamp W. Mosquito News. 1981; 41:115.
14. Swaminathan, VS. MS Thesis. Department of Mechanical & Aerospace Engineering, North Carolina State University; Raleigh, NC: 2006. Mechanics of a mosquito bite.
15. Kong XQ, Wu CW. Phys. Rev. E. 2010; 82:011910.
16. Kong X, Wu C. Adv. Mater. Res. 2011; 299-300:376.
17. Suzuki H, Tokuda T, Kobayashi K. Sensors Actuators B. 2001; 83:53.
18. Suzuki H, Tokuda T, Miyagishi T, Yoshida H, Honda N. Sensors Actuators B. 2004; 97:90.

19. Tsuchiya, K.; Nakanishi, N.; Nakamachi, E. Proceedings of the Conference on BioMEMS and Nanotechnology; Perth, Australia. 2003. p. 5257-265.
20. Tsuchiya K, Nakanishi N, Uetsuji Y, Nakamachi E. Biomedical Microdevices. 2005; 7:347. [PubMed: 16404513]
21. Tsuchiya, K.; Isobata, K.; Sato, M.; Uetsuji, Y.; Nakamachi, E.; Kajiwara, K.; Kimura, M. Proceedings of the Conference on BioMEMS and Nanotechnology III; Canberra, Australia. 2008. p. U178-U188.
22. Gattiker GE, Kaler KVIS, Mintchev MP. Microsyst. Technol. 2005; 12:44.
23. Ramasubramanian MK, Barham OM, Swaminathan V. Bioinspiration Biomimetics. 2008; 3:046001. [PubMed: 18779629]
24. Izumi H, Yajima T, Aoyagi S, Tagawa N, Arai Y, Hirata M. IEEJ Trans. Electrical and Electronic Engineering. 2008; 3:425.
25. Chakraborty S, Tsuchiya K. J. Appl. Phys. 2008; 103:114701.
26. Aoyagi S, Izumi H, Fukuda M. Sensors Actuators A. 2008; 143:20.
27. Kong XQ, Wu CW. J. Bionic Eng. 2009; 6:143.
28. Tsuchiya K, Jinnin S, Yamamoto H, Uetsuji Y, Nakamachi E. Precision Engineering. 2010; 34:461.
29. Izumi H, Suzuki M, Aoyagi S, Kanzaki T. Sensors Actuators A. 2011; 165:115.
30. Gittard SD, Narayan RJ, Ovsianikov A, Chichkov BN. Mater. Res. Soc. Proc. 2010; 1239:VV-01-11.
31. Gittard, SD.; Narayan, RJ. Toxicology of the Skin. Monteiro-Riviere, NA., editor. Vol. Chapter 29. Informa Healthcare; New York: 2010. p. 301-316.
32. Gittard SD, Ovsianikov A, Chichkov BN, Doraiswamy A, Narayan RJ. Expert Opinion on Drug Delivery. 2010; 7:1. [PubMed: 20017657]
33. LaFratta CN, Li L, Fourkas JT. Proc. Natl. Acad. Sci. USA. 2006; 103:8589. [PubMed: 16720698]
34. Lim TW, Park SH, Yang DY, Pham TA, Lee DH, Kim DP, Chang SI, Yoon JB. Microelectronic Eng. 2006; 83:2475.
35. Mukai K, Yoshimura T, Maruo S. Japanese J. Appl. Phys. Part 1. 2007; 46:2761.
36. Sun, SF.; Li, ZZ.; Wang, PP.; Huang, WH. Proceedings of the 2009 IEEE International Conference on Mechatronics and Automation; Changchun, China. 2009. p. 1427-1432.
37. Koroleva A, Schlie S, Fadeeva E, Gittard SD, Miller P, Ovsianikov A, Koch J, Narayan RJ, Chichkov BN. J. Optics. 2010; 12:124009.
38. Gittard SD, Ovsianikov A, Monteiro-Riviere NA, Lusk J, Morel P, Minghetti P, Lenardi C, Chichkov BN, Narayan RJ. J. Diabetes Sci. Technol. 2009; 3:304. [PubMed: 20144361]
39. Technical Data: EnvisionTEC e-Shell 200 Series. http://www.envisiontec.de/fileadmin/pdf/MatSheet_eShell200_en_s.pdf. Retrieved on May 29, 2011
40. Gittard SD, Narayan RJ, Lusk J, Morel P, Stockmans F, Ramsey M, Laverde C, Phillips J, Monteiro-Riviere NA, Ovsianikov A, Chichkov BN. Biotechnology J. 2009; 4:129.
41. Gittard SD, Ovsianikov A, Akar H, Chichkov B, Monteiro-Riviere NA, Stafslien S, Chisholm B, Shin CC, Shih CM, Lin SJ, Su YY, Narayan RJ. Adv. Eng. Mater. 2010; 12:B77. [PubMed: 21037972]
42. Gittard SD, Narayan RJ, Jin C, Ovsianikov A, Chichkov BN, Monteiro-Riviere NA, Stafslien S, Chisholm B. Biofabrication. 2009; 1:041001. [PubMed: 20661316]
43. Davis SP, Landis BJ, Adams ZH, Allen MG, Prausnitz MR. J. Biomechanics. 2004; 37:1155.
44. Park JH, Yoon YK, Choi SO, Prausnitz MR, Allen MG. IEEE Trans. Biomedical Eng. 2007; 54:903.
45. Kim, SC.; Shetty, S.; Price, D.; Bhansali, S. Proceedings of the 28th Annual International Conference of the IEEE Engineering in Medicine and Biology Society; New York. 2006. p. 2479-2482.
46. Khanna P, Luongo K, Strom JA, Bhansali S. J. Micromech. Microeng. 2010; 20:045011.
47. Khanna, P.; Silva, H.; Bhansali, S. Proceedings of the Eurosensor XXIV Conference; Linz, Austria. 2010. p. 5977-980.

48. Yang M, Zahn JD. Biomedical Microdevices. 2004; 6:177. [PubMed: 15377826]
49. Verbaan FJ, Bal SM, van den Berg DJ, Groenink WHH, Verpoorten H, Luttge R, Bouwstra JA. J. Controlled Release. 2007; 117:238.
50. Vemulapalli V, Yang Y, Friden PM, Banga AK. J. Pharmacy Pharmacology. 2008; 60:27.
51. Sivamani RK, Stoeber B, Liepmann D, Maibach HI. J. Dermatological Treatment. 2009; 20:156.
52. Choi, JW.; Park, IB.; Ha, YM.; Jung, MG.; Lee, SD.; Lee, SH. Proceedings of the 2006 SICE-ICASE International Joint Conference; Busan, South Korea. 2006. p. 3678-3681.
53. Choi SO, Kim YC, Park JH, Hutcheson J, Gill HS, Yoon YK, Prausnitz MR, Allen MG. Biomedical Microdevices. 2010; 12:263. [PubMed: 20012696]
54. Haq MI, Smith E, John DN, Kalavala M, Edwards C, Anstey A, Morrissey A, Birchall JC. Biomedical Microdevices. 2009; 11:35. [PubMed: 18663579]
55. Verbaan FJ, Bal SM, van den Berg DJ, Dijksman JA, van Hecke M, Verpoorten H, van den Berg A, Luttge R, Bouwstra J. J. Controlled Release. 2008; 128:80.
56. Ai-Qallaf B, Das DB. Chemical Eng. Sci. 2008; 63:2523.
57. Lee JW, Park J, Prausnitz MR. Biomaterials. 2008; 29:2113. [PubMed: 18261792]
58. Doraiswamy A, Ovsianikov A, Gittard SD, Monteiro-Riviere NA, Crombez R, Montalvo E, Shen WD, Chichkov BN, Narayan RJ. J. Nanosci. Nanotechnol. 2010; 10:6305. [PubMed: 21137723]
59. Li G, Badkar A, Nema S, Kolli CS, Banga AK. Intl. J. Pharmaceutics. 2009; 368:109.
60. Bal S, Kruithof AC, Liebl H, Tomerius M, Bouwstra J, Lademann J, Meinke M. Laser Phys. Letters. 2010; 7:242.
61. Bal SM, Kruithof AC, Zwier R, Dietz E, Bouwstra JA, Lademann J, Meinke MC. J. Controlled Release. 2010; 147:218.
62. Gittard SD, Miller PR, Boehm RD, Ovsianikov A, Chichkov BN, Heiser J, Gordon J, Monteiro-Riviere NA, Narayan RJ. Faraday Discussions. 2011; 149:171. [PubMed: 21413181]
63. Park JH, Allen MG, Prausnitz MR. J. Controlled Release. 2005; 104:51.

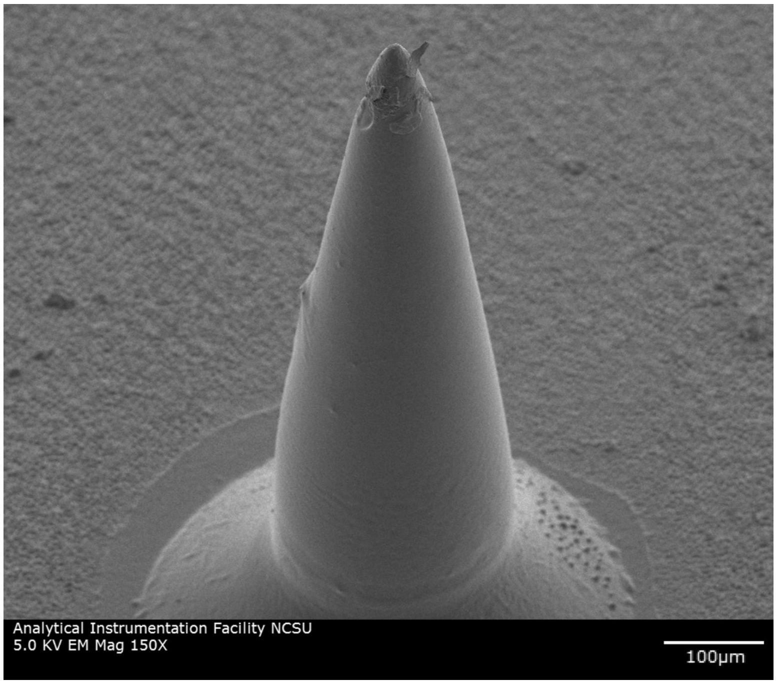

Figure 1.
Scanning electron microscopy image of a microneedle (geometry B) replica produced by an indirect rapid prototyping approach, which involved two-photon polymerization and poly(dimethylsiloxane) micromolding.

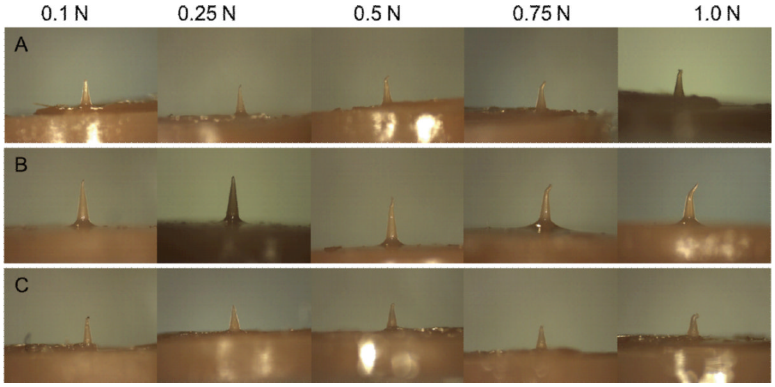

Figure 2.

Optical images of microneedles after compression testing. Microneedles with all three geometries were able to sustain compressive loads up to 0.1 N without any deformation. At 0.25 N force, microneedles with geometries B and C showed no signs of damage. On the other hand, slight deformation of the tip of the microneedle with geometry A was noted. Permanent tip deformation of microneedles with geometries B and C was observed at forces of 0.5 N and higher.

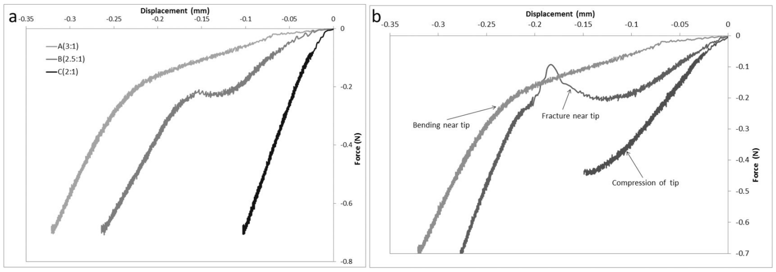

Figure 3.

Microneedle compression data. (a) Force vs. displacement plots of compressed microneedles with various aspect ratios. (b) Characteristic force vs. displacement plots showing microneedle failure mechanisms.

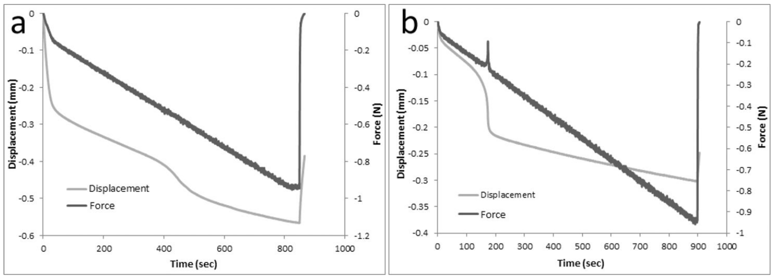

Figure 4.

Microneedle failure in force and displacement versus time: (a) bending and (b) fracturing.

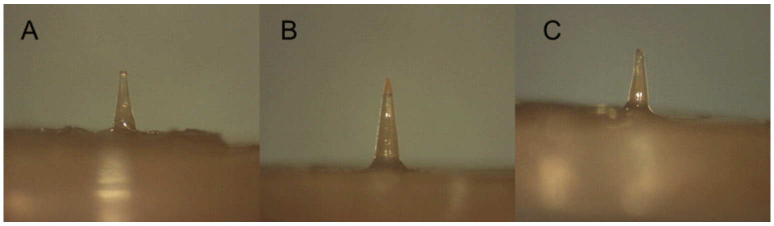

Figure 5.

Microneedles after penetrating into porcine skin with 1.0 N compression. All of the microneedle geometries were able to penetrate porcine skin without damage.

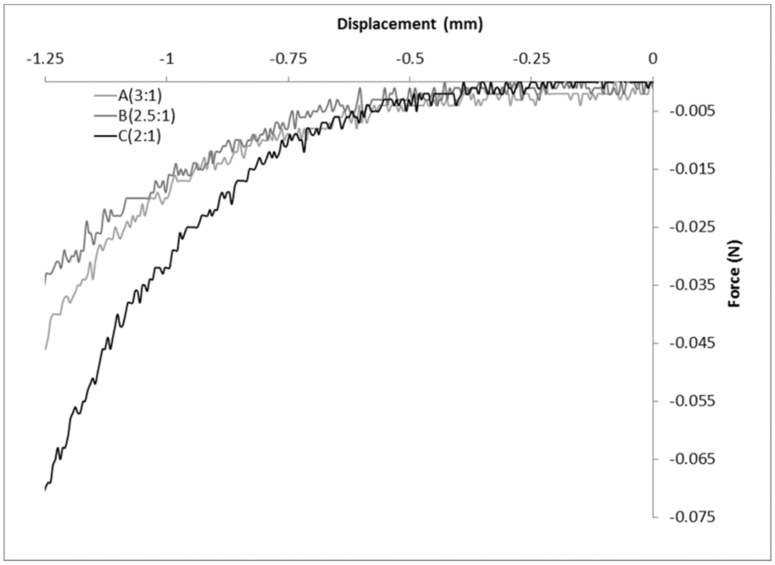

Figure 6.

Skin penetration force versus displacement for microneedle penetration of full-thickness porcine skin in displacement control mode.

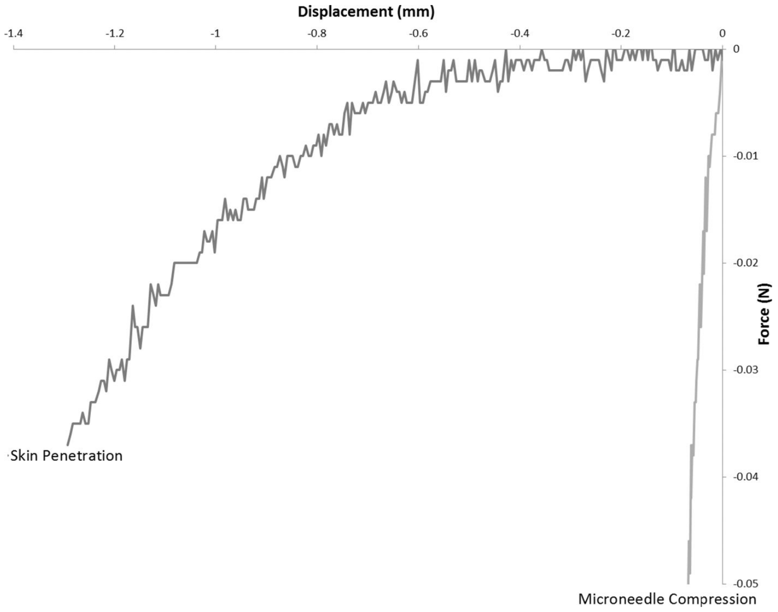

Figure 7.

Characteristic examples of force vs. displacement data for microneedles with geometry B are shown.

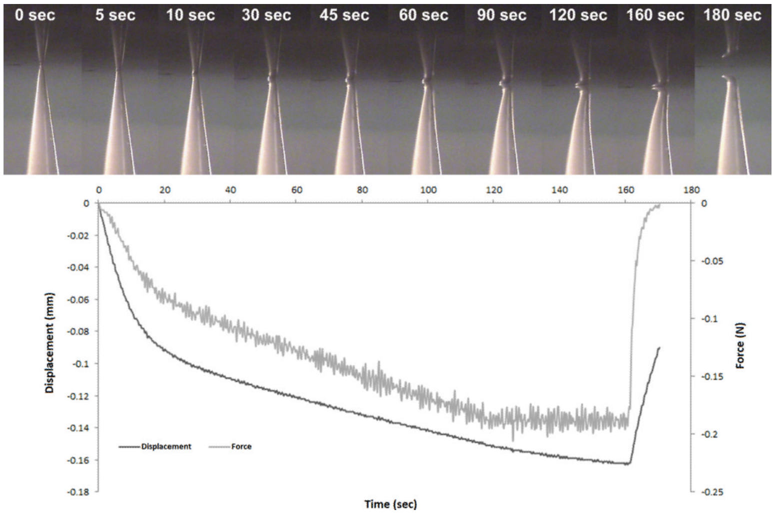

Figure 8.

Timeline of microneedle with geometry B being compressed against porcine skin in displacement controlled mode. Top: Screenshots of a video recording of the microneedle being compressed. Bottom: Force and displacement versus time during the compression.

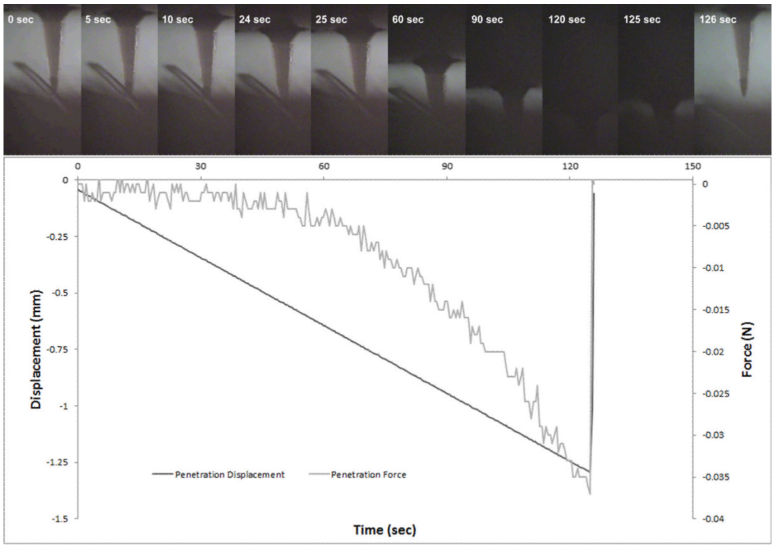

Figure 9.

Timeline of microneedle with geometry B penetrating porcine skin in displacement controlled mode. Top: Screenshots of a video recording of the microneedle penetrating porcine skin. Bottom: Force and displacement versus time during the compression.

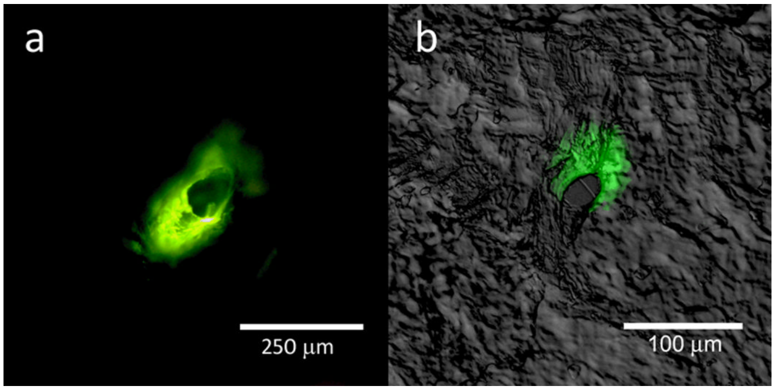

Figure 10.

Fluorescence microscopy images of lucifer yellow delivery on the porcine skin surface; confocal and differential interference contrast overlay data of lucifer yellow delivery at a depth of 120 µm are shown. The microneedle-produced pores were noted to possess irregular shapes. In addition, delivery of the lucifer yellow dye into the surrounding region of the skin was noted.

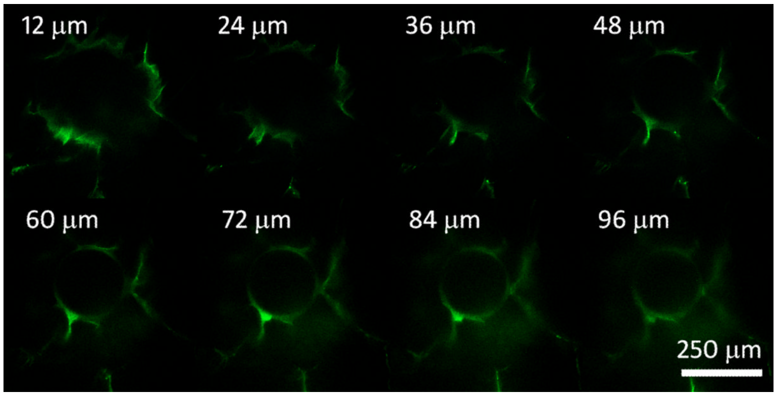

Figure 11.

Multiphoton microscopy image of lucifer yellow delivery into porcine skin. From 36 µm below the skin surface to the skin surface, the microneedle-produced pores were noted to possess an irregular shape. From 96 µm below the skin surface to 36 µm below the skin surface, the microneedle-produced pores were noted to possess a regular circular shape.

Table 1

Summary of microneedle dimensions and mechanical properties.

Designation	Base Diameter (μm)	Length (μm)	Aspect Ratio	Radius of Curvature (μm)	Stiffness (N/m)	Displacement at 0.1 N (mm)	Displacement at 0.2 N (mm)
A	250	750	3:1	10	1620 ± 1366	0.127 ± 0.117	0.182 ± 0.130
B	300	750	2.5:1	14.5	2222 ± 529	0.114 ± 0.062	0.169 ± 0.079
C	250	500	2:1	16.5	7580 ± 720	0.0255 ± 0.008	0.042 ± 0.007